Reactive Silver Inks: A Path to Solar Cells with 82% less Silver

Journal:	*Energy & Environmental Science*
Manuscript ID	EE-ART-01-2024-000020.R1
Article Type:	Paper
Date Submitted by the Author:	24-Mar-2024
Complete List of Authors:	Martinez-Szewczyk, Michael; Arizona State University Ira A Fulton Schools of Engineering DiGregorio, Steven; Colorado School of Mines Department of Mechanical Engineering, Mechanical Engineering Hildreth, Owen; Colorado School of Mines Department of Mechanical Engineering, Mechanical Engineering Bertoni, Mariana ; Arizona State University, Ira A Fulton Schools of Engineering

SCHOLARONE™
Manuscripts

Broader Context Statement for "Reactive Silver Inks: A Path to Solar Cells with 82% less Silver"

With the ever-increasing threat of global warming to life on earth, the utilization of renewable energy sources must be adopted in earnest to combat this threat. Fabricating renewable energy sources such as high-performance solar energy requires both expensive and rare materials such as silver. Silver is one of the key components that prevents the widespread adoption of solar energy into the everyday home. To meet the global demand for clean energy, the use of silver in solar modules must be decreased significantly. Using reactive silver inks in solar modules allows for up to a 82% reduction in silver consumption along with higher performance. This higher performance is enabled by the low resistivity of the reactive silver ink. Because reactive silver inks can be applied to many different emerging solar technologies, it must be better understood to take advantage of their properties and reduce the cost of solar energy.

Journal Name

ARTICLE TYPE

Reactive Silver Inks: A Path to Solar Cells with 82% less Silver[†]

Michael Martinez-Szewczyk,[*a] Steven DiGregorio,[b‡] Owen Hildreth,[b] and Mariana I. Bertoni[*a]

Silicon heterojunction (SHJ) cells currently hold the efficiency record for (c-Si) based devices of 27.09% and continue to show a promising pathway towards the practical limit of 28.5%. The efficiencies of these cells are typically limited by two main components that are closely related: the resistive losses of the contact layers across the device and the shading losses of the metallization. As the width of the contacts are reduced to minimize shading, the resistive losses of these narrower contacts become increasingly important to manage. The higher resistivity of the low-temperature silver paste (LT-SP) grid metallization is a direct result of the low temperature compatibility requirements set by the amorphous silicon layers. Reactive silver ink (RSI) coupled with dispense printing offers a path to fabricate low-temperature metallization contacts with pure metal-like properties while using 82% less silver than LT-SP (16.4 mg_{Ag} vs. 89.2 mg_{Ag}). Here we present the potential of this advanced metallization which has a unique contact geometry and can yield a total resistivity of 3.1 $\mu\Omega\cdot$cm and contact resistivity of 3.2 $m\Omega\cdot cm^2$ which results in an efficiency gain of 1.1%$_{abs}$ using an identical grid design as the LT-SP metallization. In addition, power loss analysis of the devices is performed and demonstrates how RSI metallization can achieve even higher efficiencies of 22.29%, which is 2.09%$_{abs}$ above the LT-SP baseline by redesigning the contact grid and TCO optimization.

1 Introduction

Silicon heterojunction (SHJ) solar cells currently hold the single junction crystalline silicon technology power conversion efficiency record, 27.09%[1], which is very near the practical limit of 28.5%[2]. This high performance is thanks to their low recombination losses which, as a result of their passivating layers of hydrogenated amorphous silicon (a-Si:H), results in high open-circuit voltages of well over 700 mV[3–6]. Despite these advantages, other crystalline-silicon (c-Si) solar cell architectures such as passivated emitter rear contact (PERC) and tunnel oxide passivated contact (TOPCon) still dominate the market due to their lower production cost[7–9]. The comparatively higher cost to manufacture SHJ solar cells originates from the cost of the raw materials such as the n-type silicon wafer, indium for the transparent conducting oxide, and the specialized silver paste required for metallization[10]. This specialized silver paste, which is typically screen printed, has to

be cured at temperatures lower than 200 °C in order to prevent damage to the thin layers of a-Si:H that are characteristic of the SHJ[11]. This temperature restriction is not an issue with PERC and TOPCon cells as they see temperatures of 800 °C and greater during both the firing step of the high-temperature silver paste (HT-SP) and the phosphorous diffusion of the base wafer[12].

As mentioned above, the silver paste for SHJ's must be able to form mechanically stable and conductive electrodes at the low temperatures required for SHJ cells. Due to this thermal budget, typical low-temperature silver pastes (LT-SP) contain a higher silver loading than HT-SP's in addition to solvents and curing agents[13]. The additional silver provides a connecting network of silver particles to facilitate charge extraction from the transparent conductive oxide (TCO) with minimal losses, but the solvents and other additives can interrupt this conductive network and increase the contact resistivity and overall resistivity of the resulting metallization[14,15]. The higher silver loading of the LT-SP inevitably drives up the metallization cost to 0.10 USD/W$_p$, which is double than that of technologies utilizing HT-SP and makes the SHJ architecture more susceptible to the volatility of silver pricing[16]. The cost consideration involved with the use of LT-SP will inevitably get worse as the PV manufacturing volume increases to the levels required to decarbonize the grid[17]. A study by Zhang

* E-mail: mwmarti6@asu.edu, bertoni@asu.edu

[a] Fulton Schools of Engineering, Arizona State University, 551 E. Tyler Mall, Tempe, AZ, 85287

[b] Colorado School of Mines, 1500 Illinois Street, Golden, CO, 80401

et al. demonstrated that as a result of the higher silver content in the pastes as well as the need for silver metallization on both sides of the device that SHJ's at the current silver consumption would require 117% of the global silver supply in order to reach 1 TW of production. This is over 32% more silver than TOPCon and more than double the amount of silver required to metallize PERC solar cells[13]. Zhang et al. also extended this analysis to 2031 based on silver reduction projections and resulted in 29%, 48%, and 49% of global silver supply consumption for PERC, TOPCon, and SHJ solar cells respectively. Silver consumption at this level is obviously unsustainable especially given the fact that all of PV manufacturing consumed only 14% of the global silver supply in 2022[18]. These projections are a strong incentive to replace or reduce the silver consumption and improve the electrical properties of the LT-SP because SHJ cells also serve as the preferred platform for high-efficiency silicon/perovskite tandem solar cells due to their higher open-circuit voltages, superior near-infrared response, and increased efficiency when compared to other c-Si technologies such as TOPCon and PERC cells[19–22]. Both the perovskite top and SHJ bottom cells are sensitive to increased temperatures, and as such, require a solution to the low temperature metallization issue.

Metallization for SHJ's has made several advances in recent years, namely the reduction of the finger width to sizes below 30 μm as predicted by ITRPV[8,23–25]. Figure 1a shows a comparative graph of the ITRPV silver usage projections for M2 size devices (156.75 × 156.75 mm) versus reactive silver inks and other emergent metallization technologies (Fig. 1b). It is worthwhile to note that Pingel et al. reported finger widths below the ITRPV predictions for screen printed LT-SP[26]. This study was able to achieve finger widths down to 13 μm and consume 22 mg of silver through the use of high-end screens. While this study and many more have been evaluating screen printing as the primary mode of contact deposition, innovative technologies other than screen printing have been under development to reduce silver consumption, a summary is shown in Fig. 1b. One of these technologies is the FlexTrail technology developed by Fraunhofer ISE which utilizes a thin and flexible glass capillary filled with printing medium that achieved a finger width and height of 16 μm and 0.2 μm respectively[27,28]. The low height resulted in resistive losses, and subsequent optimization of the finger cross-sectional area yielded a finger width of 29.2 μm, finger height of 6.4 μm, efficiency of 22.87%, and silver consumption of 9.4 mg which is a reduction of 68%[29]. Pospischil et al. of Highline technology GmbH demonstrated that the use of dispense printing silver paste can yield remarkable finger widths down to 17 μm for PERC cells, but due to spreading of the LT-SP resulted in finger widths of 45 μm and a silver consumption of 65 mg for SHJ cells[30]. Finally, Gensowski et al. utilized dispense printing to achieve a finger width of 41 μm and an aspect ratio of 0.4[31]. This device's silver consumption was 52 mg/cell with a power conversion efficiency of 21.5%, corresponding to an efficiency increase of 0.48%$_{abs}$ compared to traditional screen printing. Note that all of these technologies showcased in Fig. 1b correspond to a busbarless design, thus the comparison with reactive inks should be to the corresponding busbarless bar at 16.4 mg/cell (▨). All of these advances demon-
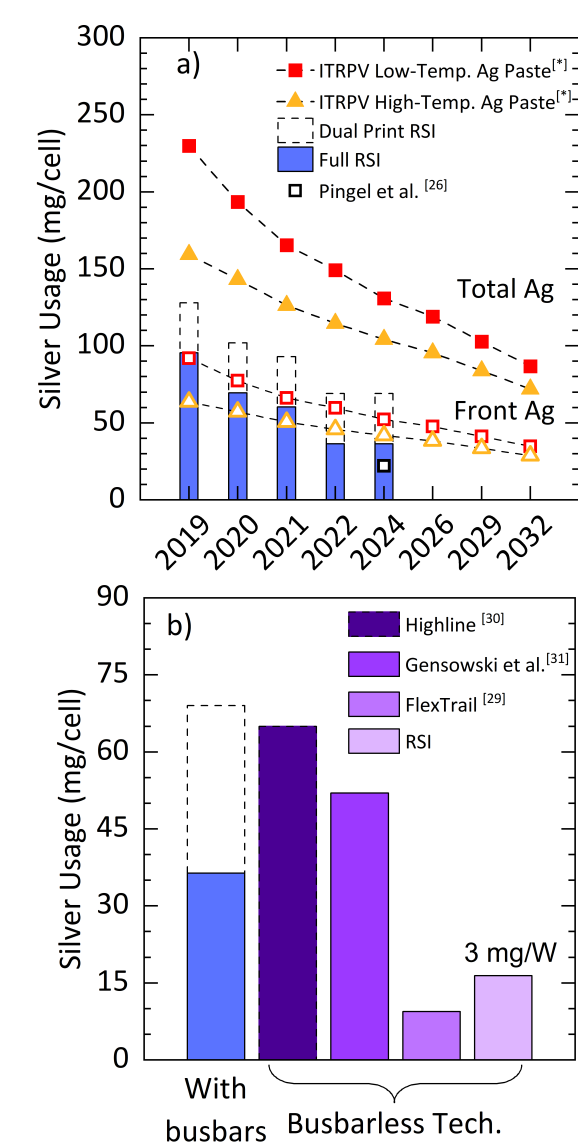

Fig. 1 a) Total silver usage for the low-temperature silver paste (LT-SP) (■) and high-temperature silver paste (HT-SP) (▲) from ITRPV[8,23–25]. Reactive silver ink(RSI) front silver usage compared to the calculated front silver usage of LT-SP (□) and HT-SP (△) from ITRPV assuming a partition of 40% front Ag. b) Inset of RSI silver usage as compared to other novel metallization schemes. It is important to note that the reported literature values for silver usage are from busbarless cells. Performing a similar comparison with the RSI, results in a very comparable front silver consumption of 16.4 mg/cell.

strate the efficacy of alternative printing methods to reduce the silver consumption for SHJ solar cells while maintaining high performance.

Our previous work has demonstrated that RSI deposited by way of dispense printing can significantly reduce the silver consumption from the resulting metallization as compared to the LT-SP[32–34]. This ink, modified from the original formulation of Walker et al.[35] relies on ethylamine as the complexing agent and was printed at 78 °C giving comparable power conversion efficiency (pce) using an identical grid design as the LT-SP paste

(18.4% and 19.5% respectively). Additionally, Mamidanna et al. studied the adhesion of RSI on indium tin oxide (ITO) and achieved improved adhesion by varying parameters such as the number of printed layers, ink dilution ratios, and droplet diameter[36]. Jeffries et al. also studied silver adhesion to the transparent conducting oxide (TCO)[37] as well as the corrosion mechanisms of reactive ink metallization and performed damp-heat reliability studies with promising results[38]. Recently, DiGregorio et al. investigated the impact of RSI formula and printing parameters on SHJ metallization[34]. The authors found that inks formulated with lower vapor-pressure complexing agents resulted in bottom-up silver growth, leading to more dense films and better electrical properties. This RSI, consisting of ethylamine, silver acetate, and formic acid was used to metallize an SHJ cell with an 84% improvement in electrical properties and 80% less silver consumption, compared to LT-SP.

Herein we expand upon these results, and study the extent of the benefits on electrical properties and power loss offered by the ethylamine RSI. SHJ solar cells were fabricated and modeled utilizing different grid designs and TCO properties to explore high performance with dramatically lower levels of silver than the state-of-the-art.

2 Methods

This study uses two ink formulations that are both based on a self-reducing RSI developed by Walker and Lewis[35]. All chemicals were used without further purification: silver acetate, anhydrous (99%, Alfa Aesar), ammonium hydroxide (28–30%, ACS grade, Sigma Aldrich), ethylamine (66–72%, Sigma Aldrich), formic acid (≥98%, ACS grade, Sigma Aldrich), and ethanol (100%, Fisher Scientific). The first formulation, referred to as ammonia ink, consisted of 2.0 g of silver acetate, 5.0 mL of ammonium hydroxide, and 0.40 mL of formic acid. This ink is Walker's original formula[35] and has been thoroughly tested for photovoltaic metallization applications through our previous publications[32–34,36,38]. The second RSI formula, referred to as ethylamine ink, was developed in our prior publication[34], and contained 0.66 g of silver acetate, 7.84 mL of ethylamine, and 0.15 mL of formic acid. For both formulas, ink synthesis began by weighing the silver acetate using an analytical balance and adding it to a plastic test tube. Next, the ammonia or ethylamine was added to the test tube and a vortex mixer was used for 30 s to ensure full dissolution of the silver acetate. Next, the formic acid was added dropwise over one minute to the test tube, and mixed with a vortex mixer for one minute. The test tube was sealed and placed in a dark environment at room temperature for 12 hours to allow any precipitated silver particles to settle. Finally, the supernatant was filtered through a 450 nm nylon syringe filter. The ink was stored at 4 °C and brought to room temperature before use. These RSI formulas do not need to be diluted and result in 5.4 ml of the ammonia ink with a silver molarity of 2.2 M, and 8 mL of the ethylamine ink with a silver molarity of 0.5 M.

The RSI was patterned using a dispense printing system[34]. The system used a syringe pump (New Era Pump Systems, NE-1010) to deliver ink at a consistent rate to the printing needle. The flexible printing needles (WPII, CMF90U) were made of fused quartz coated in polyimide and had a shaft length of 10 mm with 90 μm outer diameter and 20 μm inner diameter. The syringe pump was connected to the needles using flexible PTFE tubing (1.6 mm OD, 0.8 mm ID, Elveflow, LVF-KTU-15). The needles position was controlled using a 3-axis robot (Nordson, Pro4L). During printing, the flexible needles contacted the substrate at a 45° angle and was dragged in the opposite direction as the needle orifice. This contact printing resulted in less ink wicking and more consistent lines. The printer contained a heated stage (Instec, HCC216SF-mK2000A), that allowed for printing onto a hot substrate. Printing directly onto a hot substrate is vastly superior to post-print heat treatment schemes for self-reducing RSIs[39]. The substrate surface was at steady-state temperature before printing, and the substrates were removed from the heated stage immediately after printing. The measured substrate temperature was 105 °C for the ammonia ink and 61 °C for the ethylamine ink. No post-process heat treatment steps were used. The flow rate, print speed, number of layers, and substrate temperature were different between both ink systems due to the different silver concentrations and optimal printing temperatures. Silver consumption was calculated using the silver concentration of the formula of RSI given in mol/L along with the flow rate of the ink given in L/second. The printing speed given in mm/second and number of layers was then adjusted based on the ink properties to achieve the desired amount of silver printed. The printing parameters can be found in the SI.

The resistivity samples were created on textured Si wafers coated with 75 nm of indium tin oxide (ITO), and DC sputtered 1×1 mm Ag pads spaced 8 mm apart. The purpose of the sputtered Ag pads is to prevent damage to the RSI lines by the probe tips. Note that the resistivity samples do not contain the hydrogenated amorphous silicon layers as they are simply used to mimic the solar cell substrate for ink printing and characterization. Silver lines were printed across pads, and a Keithley 2430 1kW PULSE SourceMeter was used to measure the resistance across the pads by probing on the pads. The contribution of the conductive ITO layer was taken into account and details on the calculations can be found in the SI. The cross-sectional area of the lines was measured using a Bruker DektakXT contact profilometer. The contact resistivity samples were prepared on textured Si wafers by plasma-enhanced chemical vapor deposition (PECVD) of an intrinsic a-Si:H layer (6 nm), p-doped a-Si:H layer (17nm) followed by DC sputtering of 75 nm ITO, and 1×1 mm Ag pads spaced 8 mm apart. The full design of the fabricated samples can be found in the SI.

SHJ solar cells were fabricated from 156.75×156.75 mm (M2) 180 μm thick n-type CZ Si wafers. The wafers were then textured and cleaned in chemical baths of potassium hydroxide (KOH), RCA-B, piranha, and buffered oxide etch (BOE) solutions. Following texturing, samples had various a-Si:H layers deposited using PECVD immediately followed by DC sputtering of the front ITO, back ITO, and full-area Ag back contact. The solar cell stack is as followed from front to back: ITO 75 nm | (p) a-Si:H 17 nm | (i) a-Si:H 6 nm | (n) c-Si 150 μm | (i) a-Si:H 6 nm | (n) a-Si:H 5 nm | ITO 150 nm | Ag 200 nm. All DC sputtering was performed with a Materials Research Corporation 944 sputter-

218 ing system, and all a-Si:H deposition was performed with an IN-
219 DEOtec Octopus II system. LT-SP front grids were prepared using
220 a Baccini screen printer and Kyoto Elex silver paste (DD-1760Q
221 series) with an identical grid design as cells metallized with RSI.
222 Samples metallized with LT-SP were cured on a hotplate at 200
223 °C for 20 minutes following the manufacturer's instructions. The
224 front grid contained 66 fingers and 5 busbars for all cells. In order
225 to maintain an identical contact from the JV tester pogo pins to
226 the busbars a dual print method was utilized for the RSI printed
227 cells wherein the fingers were first dispense printed followed by
228 screen printing of the busbars with the LT-SP. This eliminated any
229 difference in the geometry of the busbars for the two types of
230 metallization in order to directly compare the performance of the
231 resulting solar cell.

232 All electrical measurements on resistivity and contact resistivity
233 samples were measured five times on five samples using the four-
234 point probe method. Solar cell characterization was performed
235 at ASU's Solar Fabrication Lab at room temperature using various
236 techniques such as external quantum efficiency (EQE): PV Mea-
237 surements QEX10, IV/Suns Voc: Sinton FCT-450 flash tester at
238 AM1.5G irradiance. Scanning electron microscope (SEM) images
239 were taken with a Zeiss Auriga SEM/FIB at an accelerating volt-
240 age of 5 kV or a Tescan Mira 3 SEM with 7 kV accelerating voltage
241 and 10 mm working distance. The measured cells were not inter-
242 connected with tabbing wire and all JV measurements were taken
243 five times on five cells using pogo pin contacts.

244 The optical properties of the fabricated cells were simulated
245 with the SunSolve Power ray-tracing software by PV lighthouse[40]
246 and matched to experimental reflectance and EQE data. The re-
247 sulting current generation profiles, which were adjusted to ac-
248 count for the differences in shading of the two types of metalliza-
249 tion, were used as inputs to simulate the electrical properties us-
250 ing the Quokka 3 software[41]. Measured device properties such as
251 lifetime curve, reverse saturation current density (J_0), contact re-
252 sistivity (ρ_c), resistivity (ρ), and shunt resistance (R_{shunt}) was also
253 measured and used to build and validate the Quokka 3 model.

3 Results and Discussion

3.1 Ink Characterization

256 Figure 2 shows the resistivity of both formulas of RSI as a function
257 of silver content versus the resistivity of the LT-SP, HT-SP[42], and
258 of bulk silver[43]. Resistivity of the metallization was calculated
259 with the following equation[44]:

$$\rho = R \cdot A/L$$

260 where ρ is resistivity, R is total resistance, A is the cross-
261 sectional area of the metallization, and L is the length of the mea-
262 sured finger segment.

263 These results show that both RSI formulations have a lower re-
264 sistivity than the LT-SP, and in some cases even lower than the
265 HT-SP. This can be explained by the difference in the pre-print
266 composition of the RSI and SP systems. The RSI precursor con-
267 tains metal ions in solution that result in a pure silver metalliza-
268 tion after printing, while the SP formulas contain binding/organic
269 agents to either aid the formation of mechanically stable contacts
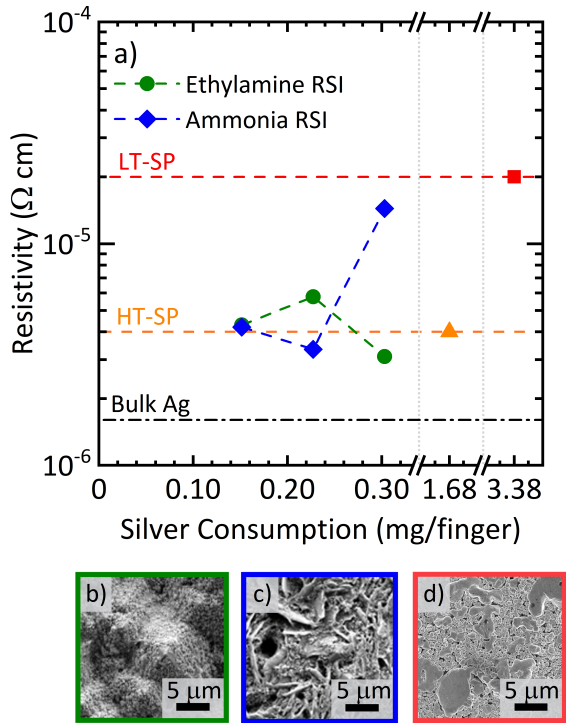

Fig. 2 Resistivity vs. silver consumption for the ethylamine (●) and the ammonia (◆) ink. Note the two axis breaks that show both formulas of RSI use less than 10% the amount of silver while maintaining reduced resistance compared to the low-temperature silver paste (■). The resistivity of the inks also rival the high-temperature silver paste (▲)[45] which require processing temperatures of up to 800 °C, whereas the RSI can be processed at 60 °C. The SEM image with a green border show that the top-down morphology of the b) ethylamine RSI is dense and has such good contact with the textured silicon substrate below that the shape of the pyramids can even be seen. This key characteristic enables its low resistivity. The SEM image with the blue border shows how subsequent printed layers of the ammonia RSI results in a much more porous and discontinuous metallization which translates to an increased resistance as compared to the ethylamine RSI. The SEM image with the red border shows that the c) LT-SP paste is also more porous which contributes to its higher resistivity. The error bars for the electrical measurements are within the marker size.

270 at low temperature in the case of LT-SP, or etch through the sil-
271 icon nitride and contact the cell absorber in the case of HT-SP.
272 Once annealed, these binding/organic agents remain in the met-
273 allization and decrease the electrical performance.

274 It is important to note that the large increase in the resistivity
275 of the ammonia ink at 0.3 mg$_{Ag}$/finger is believed to be a direct
276 result of the differences in precipitation of these two inks which
277 are described in detail elsewhere[46]. In this work, Mamidanna et
278 al. describes that the ammonia ink undergoes a top-down evap-
279 oration which forms a Ag skin at the ink-vapor interface and re-
280 sults in trapped solvent underneath. As the trapped solvent of
281 the ammonia ink begins to evaporate, it breaks the Ag skin and
282 results in a porous metallization. In an effort to control the ink
283 precipitation, DiGregorio et al. utilized an ethylamine based RSI
284 that undergoes thermal reduction at the ink-substrate interface
285 and forms a more dense and conductive film than the ammonia

ink. The 5× lower vapor pressure of the ethylamine ink impacts the rate of evaporation and subsequently the balance between evaporation (top-down) and thermally-driven (bottom-up) silver reduction[34]. It is for this reason that the ethylamine and ammonia inks were investigated to determine the feasibility of their use for solar cell contacts. Here it is important to note that the media resistivity (ρ_m), which describes the resistivity of a composite using effective media theory[47], would be more representative for the ammonia ink system but resistivity is used for simplicity and direct comparison between the two ink systems.

Figure 3 shows the decrease in contact resistivity of the ethylamine ink compared to the ammonia ink at all silver consumption values as well as the LT-SP and HT-SP[45]. All contact resistivity samples were printed using identical printing parameters as the resistivity samples and were measured according to the transfer length method (TLM)[48]. The differences between the two RSI formulations can be attributed to the precipitation methods described in the preceding paragraph as well as in detail in[34,46]. As demonstrated in the SEM images in Fig. 3, the ethylamine ink has a much more conformal and dense contact with the TCO surface which helps both validate the difference in precipitation mechanism and explain the improved contact resistivity of the ethylamine ink. As a result of these experiments and previous work, the ethylamine ink was the only RSI formulation chosen to metallize the solar cells described in this work.

3.2 Solar Cell Performance

Full-scale M2 SHJ solar cells were metallized by either RSI or LT-SP paste and characterized as described in the experimental section. The silver consumption values of 0.22 mg/finger and 0.30 mg/finger correspond to a front-grid with 15 mg_{Ag} and 20 mg_{Ag} respectively. All cells possessed an identical design of the front-grid. Fig. 4 and Table 1 show the JV performance of the RSI metallized cells with varying silver content and the LT-SP baseline cell. The V_{oc} of all precursor cells are comparable which indicates low recombination, similar amounts of potential damage to the cells from the metallization processes, and near identical passivation quality of these cells.

The lower J_{sc} of the RSI cells can be attributed directly to the difference in finger geometry of these two types of metallization. The LT-SP cell finger dimensions are 80±9 μm wide and 30±4 μm in height, while the RSI finger dimensions are 150±12 μm wide by 2±0.4 μm in height depending on the silver amount. This increase in finger width of the RSI contributes directly to shading of the solar cell and subsequently results in a reduction of the J_{sc}. Note that the width of the RSI lines are determined by the diameter of the needle; and while smaller lines can be achieved with smaller needle diameters the comparison presented here shows that the RSI's remarkable electrical properties clearly make up for the shading difference[49–52]. In order to illuminate the effect of the RSI's electrical properties on device performance, area corrected parameters are calculated to eliminate differences in shading. The ethylamine RSI cell with a front grid containing 20 mg of silver for the front grid shows the highest fill factor (FF) of 80.4% and lowest series resistance (R_s) of 0.87 mΩ cm², which
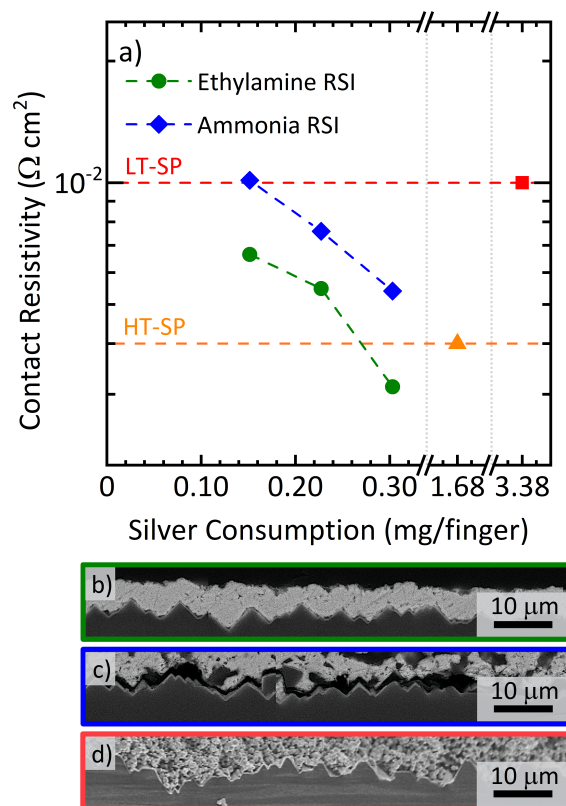

Fig. 3 a) Contact resistivity vs. silver consumption for the ethylamine (●) and the ammonia ink (◆). The contact resistivity for both ink systems decrease as a function of the amount of silver and achieve better performance than both the LT-SP (■) and HT-SP (▲) with significantly less silver usage. b) The cross-sectional SEM with a green border shows not only the dense contact formed with the ethylamine ink, but also the remarkable substrate contact due to the thermal evaporation of the ink. c) The SEM with a blue border shows how the evaporation-driven nature of the ammonia ink produces a porous metallization with poor substrate contact and increased resistivity compared to the ethylamine ink. d) The SEM with a red border shows the cross-section of the porous LT-SP contact with the textured substrate. This porosity is caused by the organic solvents evaporation process and is inherent to the technology. The error bars for the electrical measurements are within the marker size.

can be attributed to the vastly improved electrical characteristics of the inks over the paste. The RSI cells use 80% lower silver in the fingers than the LT-SP cells and as a result predominantly lie between the textured pyramids at the cell surface. It is important to reiterate that both the RSI and LT-SP cells use the same screen-printed LT-SP busbars. The dual printing of the RSI cells enables us to solely compare the performance of the metallization fingers[8,53], eliminating issues of dissimilar contact uniformity with the pogo pins of the JV tester. This results in an area-corrected efficiency (η^*) of 20.2%, 19.38%, and 21.3% for the LT-SP 3.38 mg/finger, RSI 0.22 mg/finger, and RSI 0.30 mg/finger respectively.

These results demonstrate that further reduction of finger width and optimization of the RSI front grid are the path forward for using reactive silver ink as a solar cell metallization. Taking advantage of the ink improved electrical performance would al-

Table 1 Solar Cell Electrical Characteristics of cells metallized with LT-SP and the ethylamine formula of RSI only. The measurement error originates from the error inherent to the tool. Area correction was done by calculating the metal coverage area of the cell, subtracting that value from the total cell area, and then using this corrected area to calculate the J_{sc} and η.

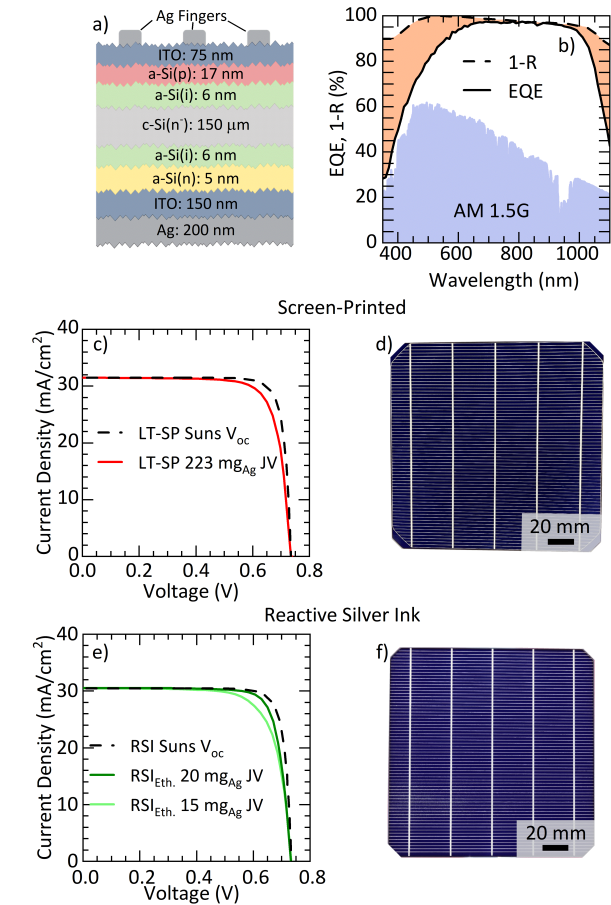|		As Measured					Area-Corrected	
	Ag Content (mg/finger)	V_{oc} (mV)	J_{sc} (mA/cm^2)	η(%)	FF (%)	R_s (Ω cm^2)	J_{sc}* (mA/cm^2)	η*(%)
LT-SP	3.38	734$\pm$3	31.48$\pm$0.16	18.06$\pm$0.06	78.11$\pm$1.2	1.45$\pm$0.14	35.2$\pm$0.13	20.2$\pm$0.05
RSI	0.22	733$\pm$2	30.50$\pm$0.14	16.54$\pm$0.06	73.94$\pm$2.3	2.4$\pm$0.22	35.70$\pm$0.11	19.38$\pm$0.07
RSI	0.30	732$\pm$3	30.54$\pm$0.13	17.99$\pm$0.05	80.4$\pm$1.1	0.87$\pm$0.12	36.1$\pm$0.09	21.3$\pm$0.04

Fig. 4 Summary of the experimental results for the SHJ solar cells. a) Architecture of the fabricated cells along with the resulting b) 1-reflection and EQE data showing the good spectral behavior of these devices. c) Suns V_{oc}, JV curve, and d) optical image of the LT-SP cell that uses 223 mg of silver. e) Suns V_{oc}, JV curves of varying silver consumption, and f) optical image for the ethylamine RSI cell. All cells demonstrate a high V_{oc}, indicating good passivation and subsequently low recombination in the device. The lower J_{sc} of the RSI is due to increased finger width of 150 μm vs. 80 μm. The RSI curve in dark green shows higher FF and lower R_s of the ethylamine RSI using 20 mg$_{Ag}$ for the fingers compared to the RSI curve in light green with a lower silver consumption. This shows the direct impact that resistivity and contact resistance have on the final device performance and confirms the superior properties of the ethylamine RSI as compared to the standard LT-SP with 80% silver.

356 low for a contact that consumes only 10% the amount of silver as
357 standard LT-SP solar cells whilst improving performance.

3.3 Solar Cell Simulation

359 The stark difference in both the contact geometry and electrical
360 properties of these metallization lends itself to the question of
361 what are the power losses associated to an optimized RSI grid?
362 To answer this, optical and electrical properties of the LT-SP and
363 RSI cells were measured as described above and used to populate
364 an optical SunSolve model and an electrical one built in Quokka 3
365 - see details in the SI. The experimentally measured JV curve of a
366 LT-SP cell plotted against a simulated curve acquired from Quokka
367 3 shows excellent agreement in V_{oc}, J_{sc}, and FF. This agreement
368 between experimental and simulated JV curves can be seen in
369 Fig. 5. Additionally, in order to eliminate any differences in shad-
370 ing between the two metallization, an RSI with an identical fin-
371 ger width as the LT-SP grid was modeled. Keep in mind that the
372 height of the RSI was also increased to 3.75 μm to maintain an
373 identical cross-sectional area and finger resistance. As can be seen
374 in Fig. 5, any issues with a low J_{sc} would no longer be a concern
375 for the RSI at identical finger widths to the LT-SP metallization.
376 The improved electrical properties of the RSI are able to shine
377 through and show the improved device performance one would
378 expect from earlier results. With the good agreement between
379 experiments and modeling, and a method to directly benchmark
380 our novel metallization, we can proceed to optimize the grid and
381 then evaluate the potential power losses.

382 As described previously, both metallization types share an
383 identical Ag grid design in order to be directly compared, but in
384 order to fully realize the potential of the RSI metallization we look
385 to take advantage of its improved electrical properties. In order
386 to do so, Griddler 2.5 software [54] was used to calculate the power
387 loss curves for various ranges of parameters such as finger spac-
388 ing and ITO layer thickness. Griddler 2.5 is a 2-D finite element
389 method (FEM) with steady state solver that can calculate the per-
390 formance of solar cells with arbitrary grid patterns. The power
391 losses include total power losses in the metallization fingers and
392 busbars as well as the optical losses. Details on the power loss
393 equations can be found in the SI. Using the single-junction SHJ
394 structure from Leilaeioun et al.[55], a Griddler model of their sys-
395 tem was built in order to compare to their results to validate our
396 model accuracy. The detailed results can be found in the SI. Our
397 calculated power losses are within $\pm$ 1.1% between the modeling
398 done in Leilaeioun et al. and the structure built using the Grid-
399 dler software for two different carrier densities of front ITO which
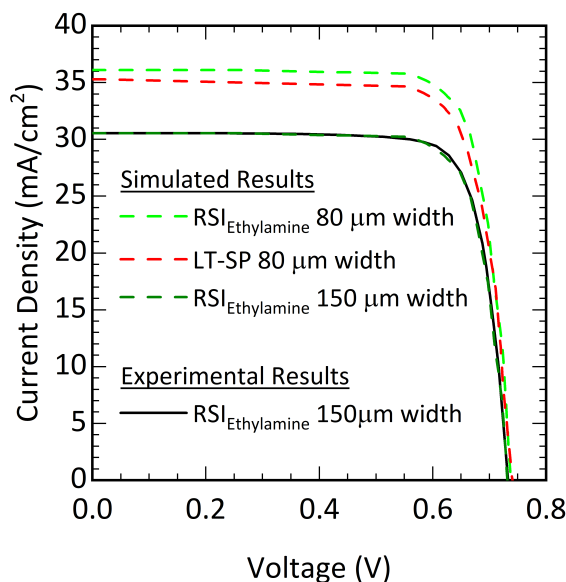400 validates the accuracy of our model.

Fig. 5 Experimental (——) vs. simulated J-V curves for an SHJ metallized with the ethylamine formula of RSI.The dashed dark green curve (- - -) shows the capabilities of the Quokka 3 software to model the performance of the RSI. The dashed bright green curve (- - -) indicates the performance simulated in Quokka 3 with an RSI finger width of 80 μm. This allows for a direct comparison between the LT-SP (- - -) and RSI metallization and demonstrates the potential of this technology to replace the standard LT-SP.
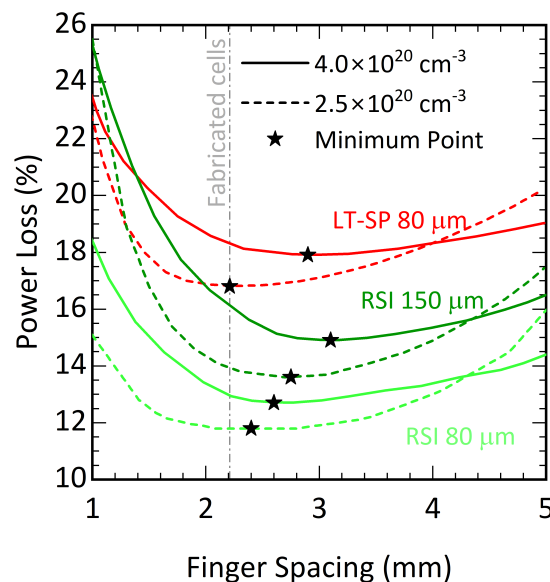

Fig. 6 Calculated power loss curves as a function of finger spacing for LT-SP with a finger width and height of 80 μm $\times$ 30 μm respectively at carrier concentrations of 4.0$\times$ 10^{20} cm^{-3} (——) and 2.5$\times10^{20}$ cm^{-3} (- - -). The ethylamine RSI metallization with a finger width of 150 μm and height of 2 μm at ITO carrier concentrations of 4.0$\times$ 10^{20} cm^{-3} (——) and 2.5$\times10^{20}$ (- - -). The ethylamine RSI at a finger width of 80 μm and finger height of 3.75 μm at the corresponding carrier concentrations (——, - - -). The dashed vertical line (- · -) indicates the grid spacing for the cells fabricated and measured above. The stars ($\star$) indicate the power loss minimum for each curve and show that the RSI must utilize a grid with higher finger spacing in order to fully take advantage of its improved electrical properties.

Using this validated Griddler model, we input the values for the ethylamine RSI at 0.3 mg$_{Ag}$/finger with a finger geometry of 150 μm $\times$ 2 μm and LT-SP with a finger geometry of 80 μm $\times$ 30 μm to obtain the power loss curves shown in Fig. 6. In Fig. 6 the minimum point for the power loss curves as a function of finger spacing are depicted as stars. Using the finger spacing of 2.21 mm and ITO carrier concentration of 2.5$\times10^{20}$ cm^{-3} which correspond to what is used in the devices above, we can see that we are at the minimum power loss for the LT-SP at 16.8% but fall short of minimizing the power loss of the RSI. A shift in finger spacing to 2.75 mm is required to reduce the power loss of the RSI to 13.6%. This shift in finger spacing corresponds to 54 printed fingers as opposed to the current grid design of 67 fingers. A cell with 54 grid fingers was fabricated and the experimental efficiency matches the simulated efficiency of 21.36%. The reduction in the number of fingers, and subsequently the power losses due to shading, are achieved as a direct result of the improved electrical properties of the RSI. The RSI's low contact resistivity reduces the amount of generated carriers that are lost when moving from the ITO to the metallization. This allows for a lower series resistance and higher spacing between fingers to be accommodated. With the optimization of the finger spacing the total silver usage for the RSI front grid fingers is 82% lower than LT-SP while improving the power conversion efficiency by up to 1.16%.

Note that the cells showcased in this work were printed using a dispense printer with a single needle and given that multiple layers are required to form a finger the throughput in a lab environment was about 3.5 hr per cell. However, there is no reason why an industrial scale dispense printer cannot hold as many needles as fingers needed. In fact, retrofitting our unit with six needles shows that printing time drops linearly to 37 min/cell. Conceivably a manufacturing scale array with several printing heads in series could achieve typical screen printing throughput of 1 sec/cell[56].

These lower power losses achieved with the RSI raise the question of whether an even more resistive TCO, with lower free-carrier absorption (FCA) could potentially be used. Hence, a range of ITO thicknesses and carrier densities were modeled to understand the extent of the RSI's electrical properties benefits.

From Fig. 7 it is clear that further reduction in carrier concentration to 1.0$\times$ 10^{20} cm^{-3} sees an increase in power loss of about 2% regardless of the metallization. This indicates that the electrical losses of the TCO, mostly driven by an increase in sheet resistance (R_{sheet}), begin to dominate as the carrier concentration reaches this lower threshold.It is important to keep in mind that even with the increased power losses at the lower ITO carrier concentration, the RSI still demonstrates similar or improved performance compared to the LT-SP at higher carrier concentrations. Additionally, in Fig. 7h, we can see that the lowest power loss of the parameter space results from a combination of an RSI metallization with decreased finger width and moderate ITO doping
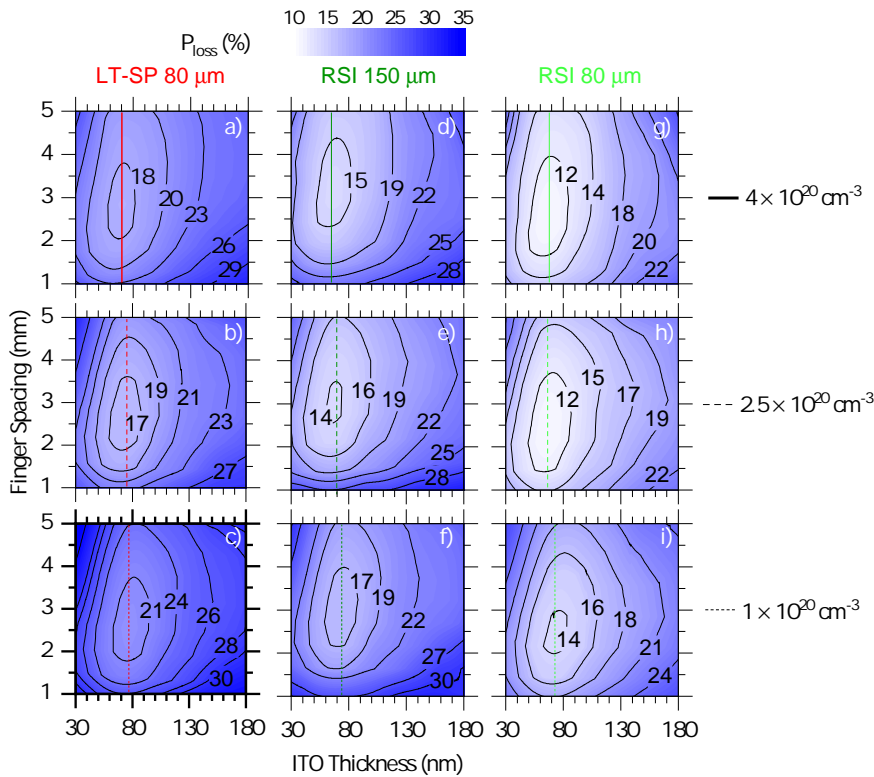
Fig. 7 Total power loss vs. finger spacing and ITO thickness for LT-SP metallization with a finger width of 80 μm and 30 μm height at ITO carrier concentrations of a) 4.0×10^{20} cm^{-3} (——), b) 2.5×10^{20} cm^{-3} (- - -), and c) 1.0×10^{20} cm^{-3} (·····). Power loss contours for RSI metallization with a finger width of d-f)150 μm and 2 μm height(——, - - -, ·····) and finger width of g-i) 80 μm by 3.75 μm height(——, - - -, ·····) with their corresponding ITO carrier concentrations. The vertical lines on each plot indicate the optimal ITO thickness at the power loss minimum for each carrier concentration. The overall trend indicates that a carrier concentration of 2.5×10^{20} cm^{-3} reduces the free carrier absorption in the film and lowers the power loss of the device, while a further reduction in ITO carrier concentration to 1 ×10^{20} cm^{-3} is dominated by poor lateral conduction in the film. The lowest power loss is achieved by the RSI with a finger width of 80 μm at a ITO carrier concentration of 2.5×10^{20} cm^{-3}.

which produces a power loss of 11.8% compared to 16.8% for the LT-SP counterpart. This 5% reduction in absolute power loss corresponds to an absolute efficiency of 22.29%. With the above results it stands to reason that the lower finger cross-sectional area and low power losses of the RSI would make it a prime candidate for a busbarless layout and could further increase the performance of this low-silver consumption technology. It is also worth mentioning that the optimal ITO thickness that leads to minimal power losses for the RSI is 69 nm as opposed to 75 nm for the LT-SP, which when combined with the lower carrier concentration could offer a further cost reduction to manufacture an RSI-metallized SHJ solar cell. The results above make a strong case for the use of RSI metallization not only on SHJ solar cells, but also on other temperature-sensitive substrates that rely on a TCO.

4 Conclusions

Herein we fabricated, quantified, and simulated the performance of utilizing a different metallization scheme for use on next-generation solar cells. This RSI metallization takes advantage of the improved electrical properties of particle free silver ink solutions that yield features with a much different geometry than traditional photovoltaic contacts. The analysis of these novel contacts demonstrated that not only can the silver consumption be reduced to 16.4 mg using an optimized front grid, TCO,reduced finger width, and busbarless technology but also improve the efficiency by 2.09%$_{abs}$ of an already high-efficiency device architecture. Additionally, it was demonstrated that out of other state-of-the-art alternatives to screen printing that also reduce silver consumption, RSI metallization consumes among the lowest amount of silver and is a prime candidate for further investigations. This large reduction in silver content is necessary to maintain the high volume of PV manufacturing without straining the limited supply of available silver and can enable terrawatt-scale production of SHJ solar cells by 2031 with only consuming ∼8% of the global silver supply. With this goal in mind, RSI metallization can be realized as a key part in reducing the cost and material consumption of photovoltaics to meet the global need for clean, renewable energy.

Conflicts of interest

There are no conflicts of interest to declare.

Acknowledgements

Notes and references

1 *LONGi Sets a New World Record of 27.09% for the Efficiency of Silicon Heterojunction Back-Contact Solar Cells*, https://www.longi.com/en/news/heterojunction-back-contact-battery/, (accessed 1 March 2024).

2 W. Long, S. Yin, F. Peng, M. Yang, L. Fang, X. Ru, M. Qu, H. Lin and X. Xu, *Solar Energy Materials and Solar Cells*, 2021, **231**, 111291.

3 S. De Wolf, A. Descoeudres, Z. C. Holman and C. Ballif, *green*, 2012, **2**, 7–24.

4 J. Haschke, O. Dupré, M. Boccard and C. Ballif, *Solar Energy Materials and Solar Cells*, 2018, **187**, 140–153.

5 M. Hermle, F. Feldmann, M. Bivour, J. C. Goldschmidt and S. W. Glunz, *Applied Physics Reviews*, 2020, **7**, year.

6 S. Bernardini, T. U. Nærland, A. L. Blum, G. Coletti and M. I. Bertoni, *Progress in Photovoltaics: Research and Applications*, 2017, **25**, 209–217.

7 M. A. Woodhouse, B. Smith, A. Ramdas and R. M. Margolis, *Crystalline silicon photovoltaic module manufacturing costs and sustainable pricing: 1H 2018 Benchmark and Cost Reduction Road Map*, National renewable energy lab.(nrel), golden, co (united states) technical report, 2019.

8 VDMA, *International Technology Roadmap for Photovoltaic (ITRPV) 2022 Results*, 2023.

9 C. Messmer, B. S. Goraya, S. Nold, P. S. Schulze, V. Sittinger, J. Schön, J. C. Goldschmidt, M. Bivour, S. W. Glunz and M. Hermle, *Progress in Photovoltaics: Research and Applications*, 2021, **29**, 744–759.

10 Z. Sun, X. Chen, Y. He, J. Li, J. Wang, H. Yan and Y. Zhang, *Advanced Energy Materials*, 2022, **12**, 2200015.

11 B. Demaurex, S. De Wolf, A. Descoeudres, Z. Charles Holman and C. Ballif, *Applied Physics Letters*, 2012, **101**, year.

12 B. Kafle, B. S. Goraya, S. Mack, F. Feldmann, S. Nold and J. Rentsch, *Solar Energy Materials and Solar Cells*, 2021, **227**, 111100.

13 Y. Zhang, M. Kim, L. Wang, P. Verlinden and B. Hallam, *Energy & Environmental Science*, 2021, **14**, 5587–5610.

14 D. Chen, L. Zhao, H. Diao, W. Zhang, G. Wang and W. Wang, *Journal of alloys and compounds*, 2015, **618**, 357–365.

15 G. Guo, W. Gan, F. Xiang, J. Zhang, H. Zhou, H. Liu and J. Luo, *Journal of materials science: materials in electronics*, 2011, **22**, 527–530.

16 A. Louwen, W. Van Sark, R. Schropp and A. Faaij, *Solar Energy Materials and Solar Cells*, 2016, **147**, 295–314.

17 *The Solar Futures Study*, 2021, https://www.osti.gov/biblio/1820105.

18 *The Silver Institute, Silver Supply and Demand*, https://www.silverinstitute.org/silver-supply-demand/, (accessed 1 March 2024).

19 J. Werner, C.-H. Weng, A. Walter, L. Fesquet, J. P. Seif, S. De Wolf, B. Niesen and C. Ballif, *The journal of physical chemistry letters*, 2016, **7**, 161–166.

20 F. Sahli, J. Werner, B. A. Kamino, M. Bräuninger, R. Monnard, B. Paviet-Salomon, L. Barraud, L. Ding, J. J. Diaz Leon, D. Sacchetto *et al.*, *Nature materials*, 2018, **17**, 820–826.

21 F. Sahli, B. A. Kamino, J. Werner, M. Bräuninger, B. Paviet-Salomon, L. Barraud, R. Monnard, J. P. Seif, A. Tomasi, Q. Jeangros *et al.*, *Advanced Energy Materials*, 2018, **8**, 1701609.

22 M. Taguchi, A. Yano, S. Tohoda, K. Matsuyama, Y. Nakamura, T. Nishiwaki, K. Fujita and E. Maruyama, *IEEE Journal of photovoltaics*, 2013, **4**, 96–99.

23 VDMA, *International Technology Roadmap for Photovoltaic (ITRPV) 2019 Results*, 2020.

24 VDMA, *International Technology Roadmap for Photovoltaic (ITRPV) 2020 Results*, 2021.

25 VDMA, *International Technology Roadmap for Photovoltaic (ITRPV) 2021 Results*, 2022.

26 S. Pingel, T. Wenzel, N. Göttlicher, M. Linse, L. Folcarelli, J. Schube, S. Hoffmann, S. Tepner, Y. Lau, J. Huyeng *et al.*, *Solar Energy Materials and Solar Cells*, 2024, **265**, 112620.

27 J. Schube, T. Fellmeth, M. Jahn, R. Keding and S. W. Glunz, *physica status solidi (RRL)–Rapid Research Letters*, 2019, **13**, 1900186.

28 J. Schube, *Ph.D. Thesis*, 2020.

29 J. Schube, M. Jahn, S. Pingel, A. De Rose, A. Lorenz, R. Keding and F. Clement, *Energy Technology*, 2022, **10**, 2200702.

30 M. Pospischil, T. Riebe, A. Jimenez, M. Kuchler, S. Tepner, T. Geipel, D. Ourinson, T. Fellmeth, M. Breitenbücher, T. Buck *et al.*, AIP Conference Proceedings, 2019.

31 K. Gensowski, M. Much, M. Palme, A. M. Jimenez, E. Bujnoch, K. Muramatsu, S. Tepner and F. Clement, *Solar Energy Materials and Solar Cells*, 2022, **245**, 111871.

32 A. M. Jeffries, A. Mamidanna, L. Ding, O. J. Hildreth and M. I. Bertoni, *IEEE Journal of Photovoltaics*, 2016, **7**, 37–43.

33 A. M. Jeffries, *Reactive Ink Metallization for Next Generation Photovoltaics*, Arizona State University, 2019.

34 S. J. DiGregorio, M. Martinez-Szewczyk, S. Raikar, M. I. Bertoni and O. J. Hildreth, *ACS Applied Energy Materials*, 2023, **6**, 2747–2757.

35 S. B. Walker and J. A. Lewis, *Journal of the American Chemical Society*, 2012, **134**, 1419–1421.

36 A. Mamidanna, A. Jeffries, M. Bertoni and O. Hildreth, *Journal of Materials Science*, 2019, **54**, 3125–3134.

37 A. M. Jeffries, Z. Wang, R. L. Opila and M. I. Bertoni, *Applied Surface Science*, 2022, **588**, 152916.

38 A. M. Jeffries, T. Nietzold, L. T. Schelhas and M. I. Bertoni, *Solar Energy Materials and Solar Cells*, 2021, **223**, 110900.

39 S. J. DiGregorio, S. Raikar and O. J. Hildreth, *ACS Applied Electronic Materials*, 2023.

40 *PV Lighthouse*, https://www.pvlighthouse.com.au/sunsolve.

41 A. Fell, *IEEE Transactions on Electron Devices*, 2012, **60**, 733–738.

42 M. A. Green, *Progress in Photovoltaics: Research and Applications*, 2011, **19**, 911–916.

43 R. A. Matula, *Journal of Physical and Chemical Reference Data*, 1979, **8**, 1147–1298.

44 Y. Singh, International journal of modern physics: Conference series, 2013, pp. 745–756.

45 H. E. Çiftpınar, M. K. Stodolny, Y. Wu, G. J. Janssen, J. Löffler, J. Schmitz, M. Lenes, J.-M. Luchies and L. Geerligs, *Energy Procedia*, 2017, **124**, 851–861.

46 A. Mamidanna, *Morphology prediction of reactive silver ink systems*, Colorado School of Mines, 2019.

47 D. S. McLachlan, M. Blaszkiewicz and R. E. Newnham, *Journal of the American Ceramic Society*, 1990, **73**, 2187–2203.

48 D. K. Schroder, *Semiconductor material and device characterization*, John Wiley & Sons, 2015.

49 C.-y. Kung, M. D. Barnes, N. Lermer, W. B. Whitten and J. M. Ramsey, *Applied optics*, 1999, **38**, 1481–1487.

50 M. Kuang, L. Wang and Y. Song, *Advanced materials*, 2014, **26**, 6950–6958.

51 H. P. Le, *Journal of imaging science and technology*, 1998, **42**, 49–62.

52 T. H. Van Osch, J. Perelaer, A. W. De Laat and U. S. Schubert, *Advanced Materials*, 2008, **20**, 343–345.

53 S. Tepner and A. Lorenz, *Progress in Photovoltaics: Research and Applications*, 2023, **31**, 557–590.

54 J. Wong and I. Zafirovska, *Griddler 2.5*, 2018.

55 M. A. Leilaeioun, A. Onno, S. Manzoor, J. Shi, K. C. Fisher, J. Y. Zhengshan and Z. C. Holman, *IEEE Journal of Photovoltaics*, 2019, **10**, 326–334.

56 S. K. Chunduri and M. Schmela, *Heterojunction Solar Technology*, 2023, https://archive.org/details/taiyang-news-report-heterojunction-solar-technology-2023.